We are IntechOpen, the world's leading publisher of Open Access books Built by scientists, for scientists

4,800
Open access books available

122,000
International authors and editors

135M
Downloads

Our authors are among the

154
Countries delivered to

TOP 1%
most cited scientists

12.2%
Contributors from top 500 universities

CLARIVATE ANALYTICS BOOK CITATION INDEX INDEXED

WEB OF SCIENCE™

Selection of our books indexed in the Book Citation Index in Web of Science™ Core Collection (BKCI)

Interested in publishing with us?
Contact book.department@intechopen.com

Numbers displayed above are based on latest data collected.
For more information visit www.intechopen.com

8

GaAs/AlOx Nonlinear Waveguides for Infrared Tunable Generation

E. Guillotel, M. Ravaro, F. Ghiglieno, M. Savanier, I. Favero, S. Ducci, and G. Leo
Laboratoire Matériaux et Phénomènes Quantiques, UMR 7162, Université Paris Diderot France

1. Introduction

New optical sources in the near- and mid-infrared (NIR/MIR respectively) have recently attracted a growing attention for potential applications in telecommunication systems (Yoo, 1996), spectroscopy (Chen et al., 1999; Arie et al., 2002), gas sensing (Lancaster et al., 1999), and quantum information (Gisin et al., 2002; Sergienko & Jaeger, 2003). In this respect, guided-wave frequency conversion is an appealing solution, due to its efficiency, compactness and tunability of the output wavelength. In this process, three guided modes coupled by the material optical nonlinearity exchange power during propagation; provided that their phase-velocity mismatch is absent or cancelled, such interaction allows the efficient transfer of power from the injected pump modes to a new-frequency generated mode, according to energy conservation (Boyd, 2008).

After the demonstration of a few original phase-matching schemes, nonlinear waveguides based on gallium arsenide (GaAs) have carved out a prominent position in the panorama of integrated frequency converters. Among their main assets, in comparison with alternative material systems: a higher nonlinear coefficient, a wider infrared transparency range, and potential monolithic integration with a laser diode pump source. On the other hand, conversion efficiency in such devices is still affected by non-negligible scattering loss, in spite of recent technological developments. Due to this limitation, no optical parametric oscillator has been reported to date in GaAs waveguides, whereas it was demonstrated long ago in lithium niobate ($LiNbO_3$) waveguides (Bortz et al., 1995).

In this chapter we focus on GaAs/AlAs nonlinear waveguides, where phase-matched three-wave mixing can be performed thanks to form birefringence. This is obtained by oxidizing a few AlAs thin layers in the waveguide core, with AlAs being transformed into a low-index non-stoichiometric aluminium oxide (hereafter referred to as AlOx). Although all different $\chi^{(2)}$ processes have been reported so far, these devices especially lend themselves to parametric down-conversion towards mid-infrared, and are promising candidates as compact sources for infrared spectroscopy. In the first section we briefly summarize the state-of-the art of mid-infrared tunable coherent sources, focusing on frequency converters. At present, none of these sources fully meets the main requirements of practical spectroscopic systems. In section two, we describe the phase-matching principle and the design guidelines of GaAs/AlOx waveguides, while the fabrication process and its crucial issues are detailed in section three.

Source: Advances in Optical and Photonic Devices, Book edited by: Ki Young Kim,
ISBN 978-953-7619-76-3, pp. 352, January 2010, INTECH, Croatia, downloaded from SCIYO.COM

The recent progress in terms of infrared generation efficiency and tunability will be the object of the fourth section. Finally, the fifth section is devoted to work in progress towards the realization of a semiconductor optical parametric oscillator.

2. Scientific context: sources for infrared spectroscopy

2.1 Laser diodes and bulk frequency converters

Mid-infrared spectrum is of strong scientific and technological interest for spectroscopy, as several molecules exhibit their fundamental rotational-vibrational resonances in this region, with absorption spectra highly specific to their atomic structure. As mid-infrared absorption lines are very strong, molecule concentrations as low as parts per-billion can be detected by means of laser-based detectors. In the near-infrared, where only overtone resonances can be excited, absorption peaks are weaker, and the corresponding detection thresholds several orders of magnitude higher. Nevertheless, many measurements are still performed at wavelengths below 2 μm, due to the relative lack of suitable laser sources at longer wavelengths. Infrared spectroscopy requires continuously tunable sources, with compactness and room temperature operation highly desirable. In the mid-infrared, the present state of the art for this type of devices includes diode lasers and sources based on nonlinear frequency conversion (Sorokina & Vodopyanov, 2003).

The main representatives of the former category are antimonide diodes and quantum-cascade lasers. Both are proven to produce significant continuous wave (CW) output power at room temperature in the 2-3 and in the 4-9 μm range, respectively, while maintaining single mode operation and being reproducibly tunable in a manner suitable for spectroscopy. Tuning is typically accomplished by changing either the temperature or the injected current, on an overall range limited to few tens of nanometres.

A versatile alternative to laser diodes is represented by sources based on $\chi^{(2)}$ nonlinear processes. For MIR generation, frequency conversion involves the use of an intense "pump" wave (generated by a laser of angular frequency ω_p), which is coupled to an input wave at ω_s (the "signal"), with an "idler" generated at the difference frequency ω_p-ω_s. The input signal photons can be provided by either a second injected laser beam or quantum noise. In the former case, the interaction is generally performed in a single-pass configuration and is referred to as difference-frequency generation (DFG). The latter process is called parametric fluorescence. Since the single-pass gain is low, it is generally exploited by resonantly enhancing the signal or the idler wave in a cavity containing the nonlinear medium, i.e. an optical parametric oscillator (OPO).

DFG and OPOs are largely employed for the generation of mid-infrared, as they can produce coherent radiation in any temporal format and over a wide spectral range, only limited by the transparency of the nonlinear crystal. For both these processes, one of the main issues is the fulfilment of the phase-matching condition. For the signal and idler waves to be continuously fed by the pump as the beams propagate through the crystal, the three waves must stay unvaried in their initial phase relation, in contrast with crystal dispersion. The classical approach to achieve phase-matched propagation consists in compensating dispersion in a birefringent nonlinear crystal. More convenient quasi-phase matching (QPM) relies on a microstructured crystals where the second-order susceptibility is periodically inverted, so as to keep the three waves into the correct phase relation. This technique, for long time the prerogative of ferroelectric crystals, further reinforced $LiNbO_3$ position as the nonlinear crystal of choice, including for the fabrication of infrared sources. The

combination of high nonlinearity and long interaction length of periodically-poled $LiNbO_3$ has considerably increased the conversion efficiency of DFG and OPO systems based on this crystal, making them accessible to diode laser or fiber laser pumping.
The implementation of QPM had an even stronger impact on GaAs. This semiconductor has a $\chi^{(2)}$ coefficient considerably higher than those of $LiNbO_3$ and of most inorganic crystals. Nevertheless, until the last decade it was not employed for frequency conversion, since it is neither anisotropic nor ferroelectric, and thus not readily suitable to the application of the above phase matching schemes. In 2001, the fabrication of the first effective QPM GaAs bulk crystals, based on lattice-matched heteroepitaxy of GaAs/Ge films on GaAs substrates (Eyres et al., 2001), rapidly opened the way for a series of tunable infrared sources with impressive performances. Among the results that followed from this technological innovation was the first GaAs-based optical parametric oscillator, reported in 2004 (Vodopyanov et al., 2004). Due to the high nonlinearity and wide transparency range of GaAs, this device was continuously tunable between 2.2 and 9 μm (limited only by mirror reflectivity), with a maximum conversion efficiency of 25%. Based on these recent results, GaAs appears to be mature as an alternative to $LiNbO_3$ for the fabrication of infrared sources.

2.2 Integrated frequency converters for the IR generation

In terms of performances, frequency converters show substantial advantages compared to laser diodes. They are suitable for oscillation from CW to femtosecond regimes, offer wider tunability ranges and great flexibility, especially since the advent of periodically poled materials. In addition, the recent demonstration of orientation-patterned GaAs promises to extend the versatility of sources based on periodically poled $LiNbO_3$ to the whole mid-infrared region. On the other hand, frequency converters are based on complex, often cumbersome setups that considerably limit their transportability, preventing their use outside of a laboratory setting. Despite the recent fabrication of miniaturized OPO sources, the degree of compactness offered by room-temperature or Peltier-cooled laser diodes remains unattainable for bulk nonlinear sources.
An intermediate solution between these two families of sources is provided by guided-wave frequency converters, which potentially combine a compactness similar to that of semiconductor lasers with the performances of frequency conversion. In general, nonlinear interactions in waveguides offer several additional features, like compactness, on-chip integration and a variety of design solutions. Moreover, the confinement of the interacting fields on a long propagation distance results in a conversion efficiency orders of magnitude higher compared to their bulk counterparts. On the other hand, the fabrication of waveguides is often technologically more complex than that of bulk crystals. The key issues are scattering losses, which can considerably limit the efficiency of nonlinear processes. In spite of such technological drawbacks, several highly-performing integrated frequency converters have been demonstrated to date. Similar to bulk crystals, periodically poled $LiNbO_3$ has played a major role also for guided-wave generation both in the visible (through frequency up-conversion) (Kintaka et al., 1996), and in the infrared (through down-conversion) (Bortz et al., 1995; Hofmann et al., 1999).
With respect to $LiNbO_3$ and dielectric waveguides in general, GaAs integrated nonlinear devices offer the additional potential benefit of the integration with a pumping source. A tangible evidence of this appeal is given by the large number of integrated frequency converters reported in the last decade. Regretfully, scattering losses have prevented GaAs waveguides from fully developing their potential to date. This is the case of quasi phase

matched AlGaAs waveguides, based on the same inversion technique of bulk orientation-patterned GaAs. The MBE growth of thin AlGaAs multilayers on GaAs/Ge templates has recently allowed the demonstration of guided-wave quasi phase matched frequency doubling (Yu et al., 2005). With a CW 1.55 μm pump, a normalized conversion efficiency η_{norm} = 92 % W^{-1} cm^{-2} was achieved, much lower than the calculated efficiency, η_{norm}=500% W^{-1} cm^{-2}. Such discrepancy arises from high scattering losses, due to waveguide corrugation at the inverted domain boundaries. The resulting attenuation coefficient is of the order of 10 dB/cm, more than two orders of magnitude higher than in GaAs bulk crystals.

At present, a performing alternative to QPM in GaAs waveguides is represented by form birefringence. This kind of integrated frequency converters, based on a strongly birefringent guiding core, were developed in the late 90's at the Thomson CSF (today Thales) laboratories. By embedding in a GaAs guiding layer several low-index AlOx layers, a form-birefringence sufficient to fulfil the phase-matching condition in the infrared was attained (Fiore et al., 1998a). As detailed in the following, AlOx layers result from the selective oxidation of AlAs layers embedded in the structure. Due to design versatility, this approach has since been successfully employed to phase match either down- or up-conversion interactions, with experimental efficiencies η_{norm} up to more than 1000% W^{-1} cm^{-2} and scattering losses lower than 1 cm^{-1} (Moutzouris et al., 2001; Ravaro et al., 2007).

From a technological point of view, in the last decade GaAs/AlOx approach has experienced a strong development. The very first conversion demonstrations suffered from processing immaturity, resulting in high propagation losses. At present, the conversion efficiency for both frequency doubling and down-conversion is comparable to that of $LiNbO_3$ counterparts. Whereas a gap still remains in terms of propagation losses, last advancements paved the way for the accomplishment of a resonant configuration.

3. GaAs/AlOx waveguides for parametric down-conversion

3.1 Form birefringence

A significant difference between TE_0 and TM_0 refractive indices n_{TE0}-n_{TM0}, referred to as modal birefringence, can e.g. be achieved by fabricating waveguides with birefringent materials, like $LiNbO_3$. Nevertheless, even in the case of optically isotropic media, waveguides are slightly birefringent, due to different boundary conditions for TE and TM polarizations. Whereas such "form" birefringence is too weak to compensate dispersion in frequency conversion processes, it can be greatly enhanced by designing a waveguide with several index discontinuities.

In a periodic multilayer stack of isotropic materials, the existence of repeated discontinuities of the refractive index along one direction breaks the original 3 axes rotation symmetry of the constituent media and results in a macroscopic negative uniaxial crystal. With reference to the geometry described in Figure 1, for plane waves in an infinitely extended medium, the ordinary and extraordinary refractive indices are equal to (Born, 1980; Yeh, 1988):

$$n_0^2 = \frac{h_1}{\Lambda} n_1^2 + \frac{h_2}{\Lambda} n_2^2$$

$$\frac{1}{n_e^2} = \frac{h_1}{\Lambda}\frac{1}{n_1^2} + \frac{h_2}{\Lambda}\frac{1}{n_2^2} \qquad (1)$$

where n_i and h_i are the refractive index and the thickness of the ith (i = 1, 2) repeated layer, and Λ the period ($h_1 + h_2 = \Lambda << \lambda$, with λ the optic wavelength). The corresponding form birefringence $\Delta n = n_o - n_e$ depends on the duty cycle and the index contrast.

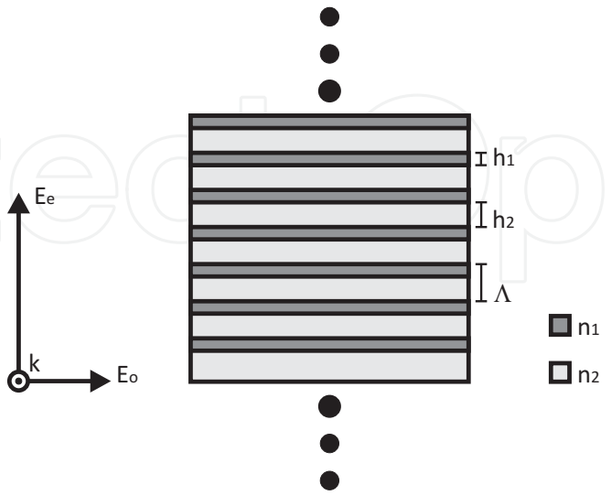

Fig. 1. Scheme of a form birefringent multilayer periodic structure.

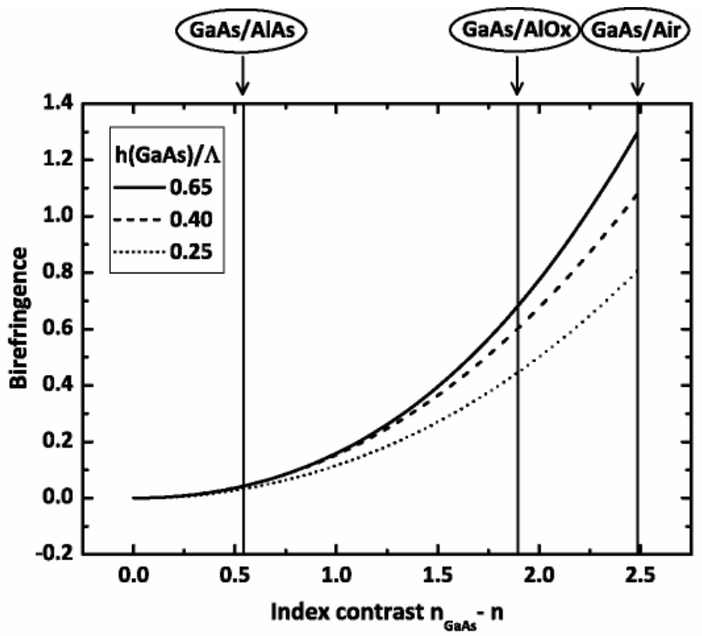

Fig. 2. Form birefringence, in plane-wave approximation, of a multilayer periodic structure of GaAs and a generic material of refractive index n, for three different duty cycles. The index contrasts corresponding to GaAs/AlAs, GaAs/AlOx, and GaAs/air combinations are pointed out.

Form-birefringent phase matching was firstly proposed in multilayer AlGaAs structures, with a birefringence suitable to perform frequency doubling in the mid-infrared, for instance from a CO_2 (λ = 10.6 μm) pump laser (Ziel, 1975; Ziel & Gossard, 1978). As maximum birefringence obtained by GaAs/AlAs index contrast is not sufficient to compensate

dispersion near the forbidden band, near-infrared phase matching is not accessible with these materials. The scenario changed in the early 90's with the demonstration of selective wet oxidation of AlAs layers embedded in GaAs (Dallesasse et al., 1990a). This process produces polycrystalline aluminium oxide layers, with a refractive index of 1.6, whose characteristics will be discussed more in detail in Section 4. The benefit resulting from the obtained index contrast is illustrated in Figure 2, which shows form birefringence for a periodic structure alternating GaAs with a lower index material.

The first achievement of form-birefringent phase matching in an AlOx-based heterostructures was demonstrated with mid-infrared difference frequency generation from two near-infrared guided waves (Fiore et al., 1997). Two continuous-wave pump lasers, a Nd:YAG at 1.32 μm and a Ti:Sapphire at 1.03 μm were end-fire coupled in a GaAs/AlOx waveguide to generate a guided mode at 4.8 μm. Afterwards, a different waveguide design allowed the frequency doubling of a CWdye-laser in the telecom range, with a conversion efficiency of η_{norm} = 4% W^{-1} cm^{-2}, mainly limited by scattering losses (Fiore et al., 1998b).

After a few years of technological development, which mainly produced a significant loss reduction, a similar device was employed to demonstrate parametric fluorescence (De Rossi et al., 2001). In that case a CW Ti:Sapphire laser was coupled into a 3.2 mm-long waveguide and, thanks to a peak efficiency η_{norm} = 1000% W^{-1} cm^{-2}, a parametric fluorescence signal around 2 μm could be detected.

3.2 Waveguide design

The main design criterion for a form-birefringent nonlinear waveguide consists in aiming at the balance between form birefringence and overall (material+waveguide) dispersion for the fundamental modes, at the frequencies involved. Further guidelines followed for the multilayer waveguide design are:

- maximization of the nonlinear overlap integral: in order to improve the efficiency of a frequency conversion process, interacting modes must have similar field distributions with as-high-as-possible peak intensities. In addition, in AlGaAs waveguides, Al content must be minimized, as AlGaAs $\chi^{(2)}$ strongly decreases with Al content.
- minimization of propagation loss: AlOx layers are the main cause for propagation losses in GaAs/AlOx waveguides, due to roughness at the interfaces with contiguous crystalline layers; their number must be kept as small as possible. Scattering reduction requires field intensity at waveguide interfaces with air be minimized as well.

It is worth noticing that the selective oxidation of an AlGaAs multilayer requires the fulfilment of a few conditions: the thickness of layers to be oxidized must be included in a certain range, between a few tens and a few hundreds of nanometres, for technological reasons; in addition, as oxidation concerns not only AlAs but AlGaAs with high Al content, all layers that are not supposed to be oxidized must have an Al content lower than a certain minimum value (Dallesasse et al., 1990a; Dallesasse et al., 1990b)

Dispersion compensation in the near- and mid infrared requires a form birefringence of few tenths (0.2-0.3), lower than the value calculated in plane-wave approximation for the index contrast n_{GaAs}-n_{AlOx} (see Figure 2). This allows increasing the period Λ (and reducing the number of AlOx layers) beyond the long-wavelength range (Λ << λ), in order to limit scattering losses. Thus, the multilayer design for a given frequency conversion process is based on the number of AlOx layers necessary to compensate dispersion for the set of wavelengths concerned. Accordingly, the fabrication of frequency converters operating close to GaAs forbidden band is more critical, due to large number of AlOx layers required.

That is why up- and down-conversion schemes between 0.75 μm and the telecom range have been abandoned, after the first frequency doubling report. Hereafter we refer to GaAs/AlOx waveguides for parametric down-conversion from a 1 μm pump. Such design has led to the most recent relevant results, and is retained as the basis for the fabrication of an optical parametric oscillator.

According to GaAs selection rules for waveguides grown on standard (001) GaAs substrates, second order nonlinear interactions are only possible between a combination of two TE modes and one TM mode. As form birefringence results in a lower refractive index for the polarization orthogonal to the layers plane, i.e. TM, the only possible phase matching scheme in this geometry is a type I with a TM polarized pump. The phase-matching condition for parametric generation at degeneracy reads

$$n_{TM_0}(1\mu m) = n_{TE_0}(2\mu m) \tag{2}$$

which implies that birefringence at 1 μm must compensate TE_0 overall dispersion between 1 μm and 2 μm:

$$\underbrace{n_{TE_0}(1\mu m) - n_{TM_0}(1\mu m)}_{\text{Birefringence}} = \underbrace{n_{TE_0}(1\mu m) - n_{TE_0}(2\mu m)}_{\text{Dispersion}} \tag{3}$$

For a core thickness resulting in single-mode confinement for the pump, the fulfilment of eq. 3 requires the introduction of five thin AlOx layers in the GaAs core. The thickness of the interposed GaAs layer is then set as to precisely tune the phase-matched set of wavelengths. The structure design for 1.064 μm pumping at degeneracy is described in Table 1. Figure 3 shows the corresponding refractive index profile, along with the resulting intensity profiles of the interacting modes at degeneracy. Here, the form birefringence principle is pointed-out: the TM polarization, parallel to the growth direction, is enhanced in the low index layers, due to electric displacement vector conservation at the interfaces. On the other hand, the TE polarization field is continuous on at the same interfaces. As a consequence, the TM effective index is significantly reduced, while the TE one stays almost unchanged.

Lateral optical confinement is then obtained by etching 3 μm wide ridges in (110) direction. Note that, for such width, the phase-matching condition calculated for the planar structure is just slightly red-tuned. If needed, ridge width can be adjusted to correct a phase-matching wavelength shift due to growth inaccuracy.

For such a device the calculated parametric gain coefficient, normalized to the root of the power, is $g/P^{1/2} = 4.8\ W^{-1/2}cm^{-1}$ at degeneracy. The generated signal and idler wavelengths can then be tuned on a wide spectral region by reducing the pump wavelength with respect

	Composition	Thickness (nm)
	GaAs	Substrate
	$Al_{0.7}Ga_{0.3}As$	1000
	AlOx	33
4×	GaAs	273
	AlOx	33
	$Al_{0.7}Ga_{0.3}As$	1000
	GaAs	30

Table 1. Multilayer structure for 1.064 μm pumping at degeneracy

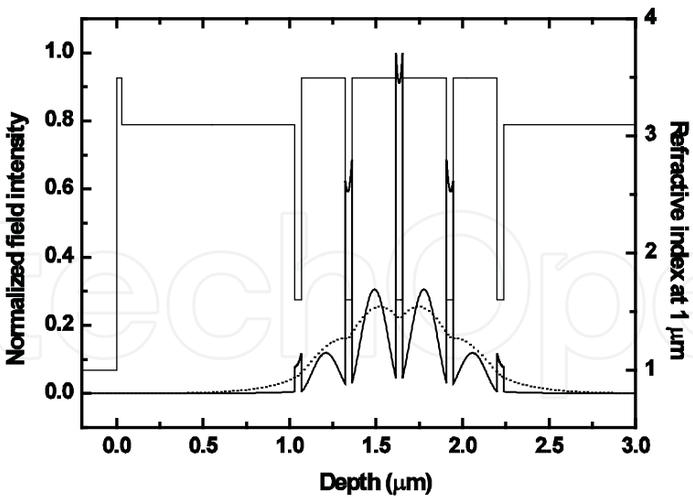

Fig. 3. Vertical structure of the form birefringent parametric generator: refractive index (thin solid line), TM_0 (thick solid line) and TE_0 (dotted line) modal profiles at λ_p = 1.064 μm and λ_s = λ_i =2 λ_p , respectively.

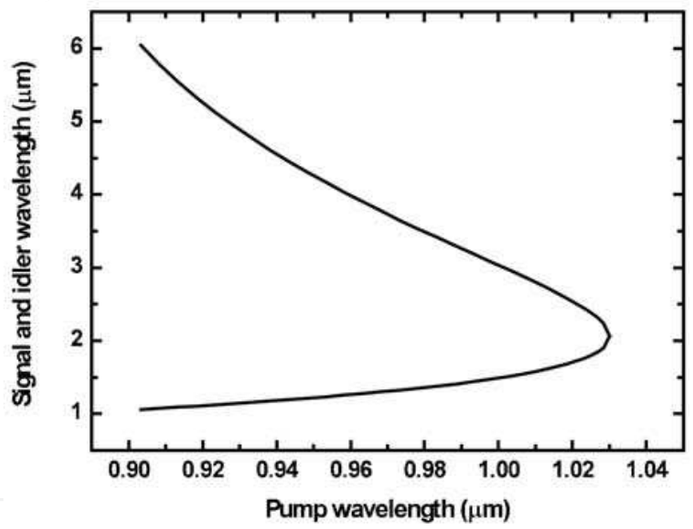

Fig. 4. Calculated parametric generation tuning curve.

to degeneracy (Figure 4). Compared to typical bulk nonlinear crystals, wavelength tuning in this geometry is highly sensitive to pump wavelength. This peculiarity stems from the huge waveguide dispersion at λ_p, much larger than at 2 λ_p, as clarified by the approximated expression for the relationship between λ_p, λ_s, and λ_i around degeneracy (De Rossi et al., 2005a):

$$\lambda_{s,i} = \frac{2\lambda_p}{1 \pm \alpha \sqrt{\frac{\lambda_p^0}{\lambda_p} - 1}} \tag{4}$$

where the "aperture" α of the tuning curve is given by

$$\alpha = \sqrt{\frac{\frac{\partial n_{TM_0}}{\partial \lambda}(\lambda_p^0)}{\frac{\partial n_{TE_0}}{\partial \lambda}(\lambda_s^0)}} \tag{5}$$

In both expressions, the superscript 0 indicates values at degeneracy. Eqs. 4 and 5, which are obtained by neglecting the second-order derivatives of the effective indices, show how a higher $(\partial n_{TM0}/\partial\lambda)/(\partial n_{TE0}/\partial\lambda)$ ratio implies a wider aperture of the tuning curve. A wide aperture α is strongly desirable for a tunable source, especially in the perspective of integrating a pump laser diode, usually exhibiting limited tunability. In addition, waveguide strong dispersion leads to somewhat reduce the down-conversion phase-matching bandwidth, typically much wider than in type II processes, especially at degeneracy.

4. Fabrication of GaAs/AlOx waveguides

Despite high nominal values, the efficiency of GaAs/AlOx nonlinear waveguides has been limited so far by high propagation losses. These arise mainly from scattering at AlOx layers interfaces. Hereafter we briefly describe the origin of this problem and the fabrication improvements we have introduced with respect to the state of the art.

4.1 Growth and lithography

The growth of GaAs/AlAs waveguides is done by molecular beam epitaxy (MBE) for its performances in terms of:

1. precision on the layer thicknesses: this is crucial to achieve a given phase-matching wavelength;
2. abruptness of the layer interfaces: a key issue to limit scattering losses following from oxidation of AlAs layers.

A single narrow ridge is chemically etched for lateral confinement and oxidation. Thanks to the low superficial roughness achieved, the adoption of deeply-etched narrow structures for lateral guidance does not imply a degradation of the waveguide transmission due to scattering at ridge sidewalls.

Initially employed for chemical etching, H_2SO_4:H_2O_2:H_2O solution has been successively replaced with the more performing HBr:CH_3COOH:$K_2Cr_2O_7$. Besides being less selective, the latter reduces under-etching and, above all, further improves etched surface smoothness. A surface analysis at the atomic force microscope has revealed a roughness reduction from 3 to 2 nm rms. This amelioration represents an advantage also for the oxidation process. Indeed, a smoother AlAs/air lateral interface is supposed to improve oxidation kinetics, allowing a better flux of H_2O toward the ridge core and a better release of reaction products.

It is worth comparing the above roughness values with those recently reported for strongly confining AlOx waveguides obtained by e-beam lithography + chlorine plasma etching (Scaccabarozzi et al., 2006). In this case, a 6 nm rms roughness is measured on the ridge sidewalls suggesting that, in spite of recent improvements, plasma-assisted etching does not provide yet the same surface quality as wet etching. The latter, in spite of poor control and reproducibility, remains a reasonable choice when low propagation losses are a priority.

4.2 Selective oxidation

AlAs, or more precisely, AlGaAs with high Al molar fraction gets easily oxidized if exposed to air. (Dallesasse et al., 1990b) The resulting oxide is unstable and causes the material to crumble. This process thus severely affects the performances of AlGaAs devices, such as lasers and more in general waveguides, containing Al rich layers. In the early 90's, an attempt to accelerate this process in a wet atmosphere at high temperature, led to demonstrate the formation of a stable native oxide (Dallesasse et al., 1990a). The so obtained aluminum oxide, AlOx, exhibits a refractive index much lower than that of AlGaAs and it is electrically insulating.

A buried thin AlGaAs layer can be oxidized starting from the etched sidewalls of the waveguide. Oxidation kinetics and, structure and characteristics of the final oxide, are very sensitive to the different parameters involved (thickness of the AlGaAs layers, Al rate, oxidation temperature).

Optical properties of AlOx have been characterized with discrepancies in the published results. AlOx transparency region has been unambiguously demonstrated to extend from deep UV (about 240 nm) up to 10 μm, (Bravetti et al., 1998; Hall et al., 1999) excepted an O-H absorption peak that we identified at 3 μm (Ravaro et al., 2008). However several different values of the AlOx refractive index have been reported. In the NIR these are included between 1.55 and 1.64, with a claimed dependence on the original Al composition. (Knopp et al., 1998; Hall et al., 1999; Durand et al., 2003) This is a major issue for the design of birefringent GaAs/AlOx nonlinear waveguides, as uncertainty on these properties affects the phase-matching wavelength of such devices.

Selective oxidation of GaAs/AlAs waveguides is carried out in a quartz tube oven where samples are heated at 420-430°C while the atmosphere is saturated in water vapor by a 2 l/min flux of wet N_2. This is obtained by previously making dry N_2 pass through a water bubbler stabilized at 70 °C.

This solution and the above novel processing technique have allowed us to further improve the transmission characteristics of GaAs/AlOx waveguides with respect to the best results previously reported. (De Rossi et al., 2001) This has been demonstrated by systematic losses measurements.

4.3 Propagation loss

Compared to gradual index dielectric waveguides, high-index-contrast semiconductor waveguides are significantly affected by scattering losses. Scattering can originate from roughness on either the ridge sidewalls or the epitaxial layers interfaces, as well as from bulk media inhomogeneity.

Scattered light measurements in AlOx waveguides, with a femtosecond NIR OPO, have allowed determining the dependence of propagation losses on wavelength (Venugopal Rao et al., 2003). In the range from 1.3 to 2.1 μm, losses were found to decrease with wavelength, as expected for Rayleigh scattering, confirming the dominant contribution of AlOx/GaAs interface roughness to the attenuation coefficient.

Waveguides propagation loss can be evaluated by the Fabry-Pérot technique (De Rossi et al. 2005b). This resorts to Fabry-Perot transmission fringes in the waveguide to infer the attenuation coefficient independently on input coupling efficiency. Due to the modal reflectivity at input and output facets, the transmission of a waveguide can be treated analogously to that of a Fabry-Perot resonator in plane-wave approximation. In a single-mode waveguide, for a monochromatic input, the transmission is given by the Airy function:

$$T_{FP} = \frac{T^2 e^{-\alpha L}}{(1-R')^2 + 4R'\sin^2(\Phi/2)}\eta \quad (6)$$

where α is the modal attenuation coefficient, L the waveguide length, η the coupling efficiency, T (R) the transmission (reflectivity) of the two facets (supposed to be equal), and $R' = R \cdot \exp(-\alpha L)$. T_{FP} is a periodic function of the round-trip dephasing $\Phi = 2k_0 N_{eff} L + \Phi_0$, with k_0 the free-space wave vector and N_{eff} the effective index. By tuning the input wavelength or the effective index (by e.g. varying the sample temperature), T_{FP} oscillates between a maximum T_{max} and a minimum T_{min} that depend only on R'. By measuring the contrast of the transmission fringes:

$$K = (T_{max}-T_{min})/(T_{max}+T_{min}) \quad (7)$$

R' is given by the relation

$$R' = \frac{1-\sqrt{1-K^2}}{K} \quad (8)$$

If the facet modal reflectivity R is known, the attenuation coefficient can finally be calculated as

$$\alpha = \ln(R/R')/L \quad (9)$$

In form birefringent GaAs/AlOx waveguides, current typical lowest propagation loss is in the order of 0.4-0.6 cm^{-1} after oxidation as compared to ≈ 0.1 cm^{-1} before oxidation. Understanding the origin of such losses is thus essential for its reduction. Taking into account the small thickness of the AlOx layers, Transmission Electron Microscopy (TEM) is the best suited instrument to quantify the GaAs/AlOx interfaces roughness.

4.4 Interface roughness characterization by transmission electron microscopy

The fabrication of cross-section specimens for transmission electron microscopy (TEM) is performed with a JEOL Ion Slicer allowing the thinning of one waveguide by sample thanks to 8 keV Ar^+ ion beam with an incident angle of 1.3°. A 2 keV Ar^+ beam at 1.0° final polish ensures minimization of surface amorphous material. The obtained foils are analysed in a JEM 2100F TEM field emission gun TEM operating at 200 kV. Thickness mapping is done for each thin foil, using a Gatan Imaging Filter with 3mm aperture and the two window-based jump ratio imaging technique (Hofer et al., 1995). Exposure time is 1 s for slit widths of 10 eV, with a beam collection angle of 11.0 mrad defined by the objective aperture. For the interfaces characterization we use the high angle annular dark field (HAADF) STEM imaging where the incoherently scattered electrons collected to produce an image are sensitive to variation of the atomic number of atoms in the sample. An example of such image is showed on figure 5.

To accurately measure the amplitude of the roughness, the following procedure is done: (I) binary contrast enhancement of the HAADF image; (II) boundary tracing; (III) line matrix averaging; (IV) gradient removal; and (V) autocorrelation analysis.

Binary contrast enhancement (I) relates to the unique identification of the delineated boundary on either side of which occurs a brightness change for the adjoining of GaAs and AlOx. A median brightness level is identified such that image pixels brighter (higher stored values) than the median will be denoted as 1, and darker image pixels (lower stored values)

are denoted as 0, thereby giving a binary image. The median can be deduced in one of two ways; by performing a trace across the image, perpendicular to the GaAs/AlOx interface, to determine the different brightness levels on either side of the boundary, or by determining the median in an image brightness intensity spectrum.
Boundary tracing (II) is next employed to digitally extract the coordinates of the interface through an algorithm that first determines a point at the interface and then follows the boundary, now defined by 0 and 1, in a systematic manner across the image from left to right. The interface coordinates are stored in a separate array.
Such vertical line matrix averaging (III) has been performed with the data being further subject to a linear least squares fit to remove any gradient (IV) displayed. Finally (V), it is possible to calculate the autocorrelation function R(u) of the interface profile defined by the function f(z): $R(u)=\langle f(z)f(z+u)\rangle$. A gaussian fit of the autocorrelation function leads to the mean square perturbation, $\sigma^2=R(0)$, of the boundary and its correlation length L_c. In the present case, values of $\sigma^2= 0.16$ nm^2 and $L_c=44$ nm were determined. The non-vanishing thickness of the TEM samples results in a fictitious smoothing of f(z) responsible of a diminution of those parameters evaluated at 39±18% and 20±20% for σ^2 and L_c respectively (Goodnick et al., 1985).

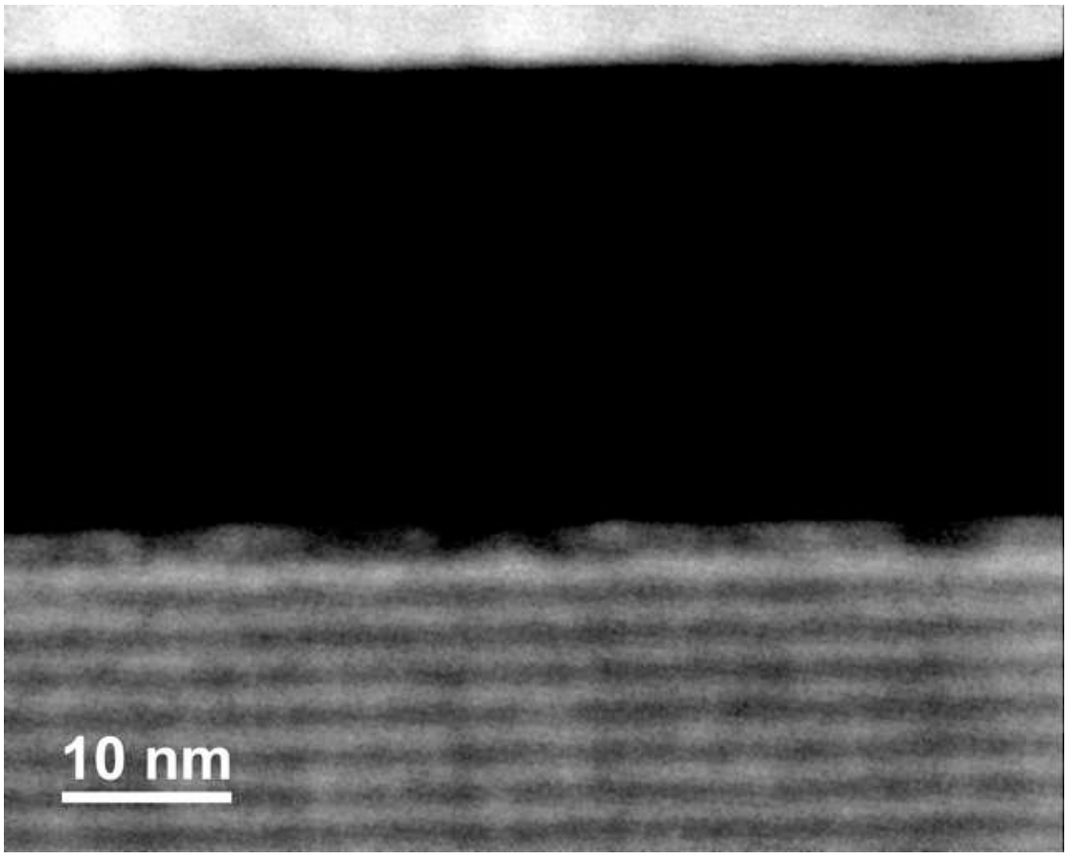

Fig. 5. HAADF image of an AlOx layer (in black) embedded in GaAs (top) and $Al_{0.7}Ga_{0.3}As$ (bottom). Rough interfaces are clearly visible with an enhanced effect at the bottom interface.

To infer Rayleigh scattering loss coefficient from these values, we adapted Lacey and Payne's simple model (Lacey & Payne, 1990) to our multilayer waveguide where the attenuation coefficient is linked to $\tilde{R}$, the Fourier transform of the autocorrelation function R(u), through the expression:

$$\alpha_r = \Phi^2(d)(n_2^2 - n_1^2)^2 \frac{k_0^3}{4\pi n_1} \int_0^{\pi} \tilde{R}(\beta - n_2 k_0 \cos\theta)\, d\theta \tag{10}$$

where n_1 and n_2 are the refractive indices of AlOx and GaAs respectively, k_0 is the wave vector in vacuum, β is the propagation vector, θ is the photon scattering angle as regards as the interface and $\phi(d)$ is the energy distribution of the propagating mode evaluated at the position of the different interfaces and normalized as follow:

$$\int_{-\infty}^{+\infty} \Phi^2(y)\, dy = 1 \tag{11}$$

Figure 6 illustrates the variation of the loss coefficient with the value of σ^2 and L_c in the case of our GaAs/AlOx waveguides. The star marks the value of the loss coefficient deducted from our TEM observations and the rectangle symbolizes the value of the loss coefficient, taking into account the effect of smoothing occurring through the pass of electrons in the thin foil. Our model gives a value for the propagation loss α=0.28±0.12cm^{-1}. This value is in fair agreement with experimental data suggesting that Rayleigh scattering could be the main source of propagation losses.

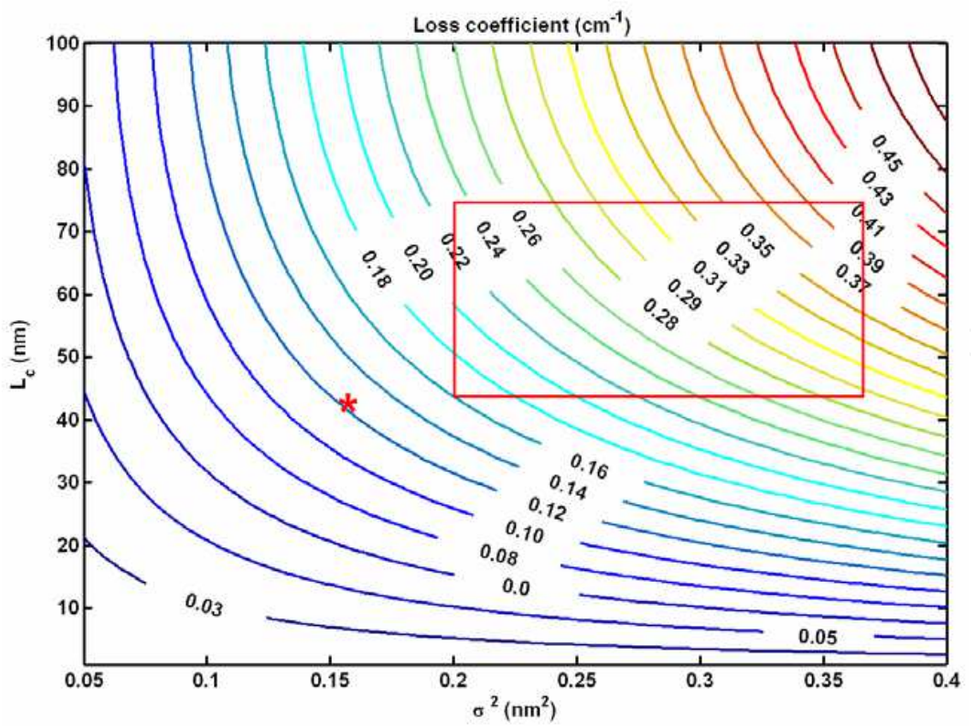

Fig. 6. Variation of the loss coefficient with the mean square value of roughness and the coherent length.

5. Experimental performances

In the first reports of form-birefringent frequency conversion, scattering losses did not allow the full exploitation of the huge normalized conversion efficiency. After the last technological advancements described above, this is now possible in mm long devices, with overall conversion efficiencies comparable to that of $LiNbO_3$ waveguides. Current loss level still prevents the use of cm long devices, which would result in even higher single-pass efficiency and make parametric oscillation more easily accessible.

In the following we present the last advancements of parametric down-conversion in mm long GaAs/AlOx waveguides. In section 5.1 we describe parametric fluorescence results, with a tuning range in excess of 1 μm. In section 5.2 we detail the first parametric amplification demonstration, which, in passing, has led to a precise determination of the parametric gain coefficient.

5.1 Parametric fluorecence

The experiment we report here was performed with a tunable Ti:Sapphire CW pump laser with 40 Ghz linewidth. The beam was TM polarized and coupled with a 60× microscope objective in a GaAs/AlOx waveguide designed for phase-matching at 1.064 μm. Waveguide length was L = 3 mm. Its output was collimated with an identical objective and passed through an high-pass interferential filter before being injected into a spectrometer equipped with an strained InGaAs photo-diode, whose cutoff limited the wavelength detection range at 2400 nm.

Two parametric fluorescence spectra, at degeneracy and 0.2 nm off degeneracy, are reported in Figure 7. Besides the good signal-to-noise ratio, their sinc^2 shape demonstrates the high uniformity of the waveguide over a few millimeter length. By acquiring parametric fluorescence spectra for different values of λ_p the tuning curve shown in Figure 8 (crosses) was reconstructed. Idler wavelengths longer than 2400 nm were inferred from measured signal and pump wavelengths, through frequency conservation. A tuning range between 1.69 μm and 2.75 μm has been obtained, limited by loss experienced by the idler mode beyond 2.75 μm. In this spectral region AlOx exhibit an absorption band which is ascribed to an Al hydroxide produced during wet oxidation (Ravaro et al., 2008). However, AlOx layers are expected to be dehydroxylated through a proper thermal annealing, thus giving access to a broader tuning range.

The experimental tuning interval above has been covered by varying λ_p over a 12 nm interval, with degeneracy at λ_p = 1060.5 nm, slightly shorter than the nominal value (λ_p = 1064 nm). These data can be reasonably fitted by a curve (solid line) obtained from effective-index calculations for the planar structure, with the thickness t of GaAs layers as fit parameter (t_{fit} = 271 nm, instead of nominal t = 273 nm). This calculated tuning curve differs from its experimental counterpart for a slightly lower tuning aperture, as determined with Eq. 4: α = 2.14 for the experimental points, versus α = 1.92 for the fitting curve. We ascribe such difference to the narrow lateral confinement of the ridge, which increases the dispersion of the waveguide and thus the aperture of the tuning curve, with respect to the results of 1D modeling.

Parametric tuning can also be obtained by changing the sample temperature, as shown in Figure 9. Here experimental data are compared with a simulated curve based on AlGaAs thermorefractive coefficients (Gehrsitz et al., 2000).

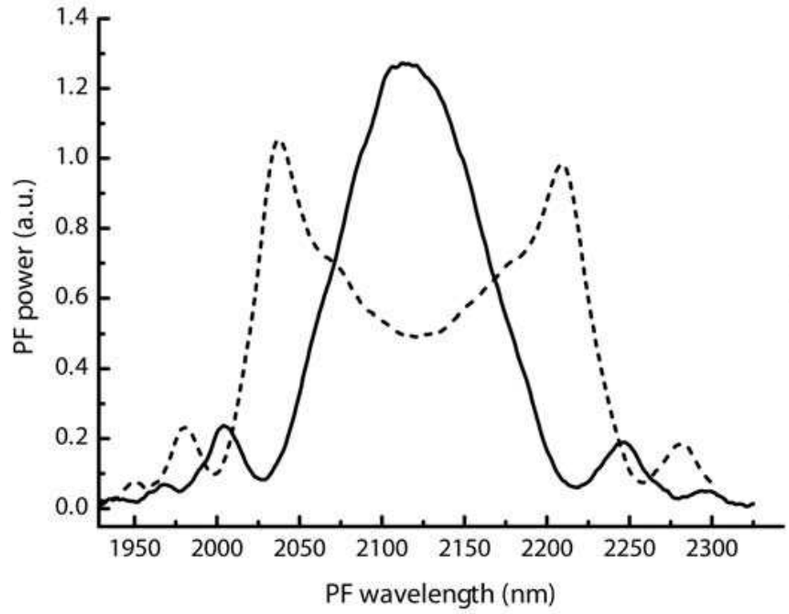

Fig. 7. Parametric fluorescence experimental spectra: at degeneracy (solid line) and 0.2 nm off degeneracy (dashed line).

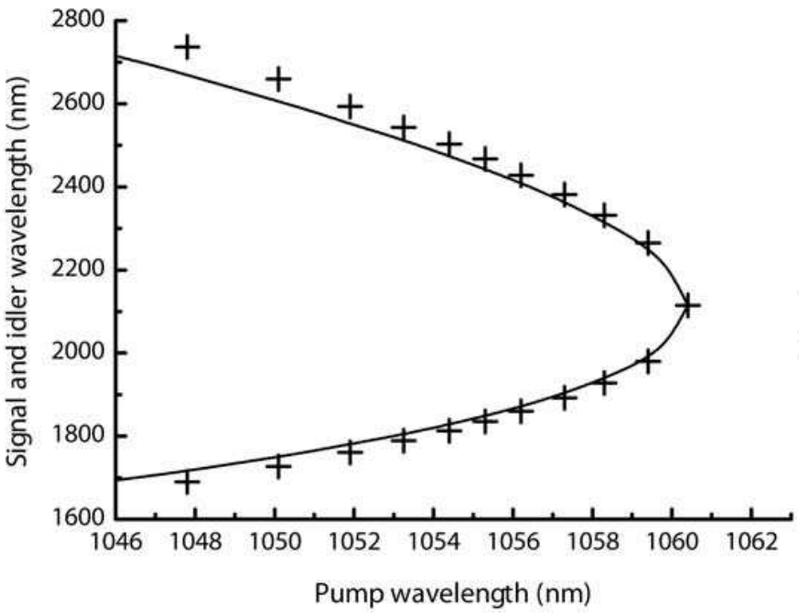

Fig. 8. Parametric fluorescence tuning curve: experimental data (+) and fitting curve for a GaAs thickness t = 271 nm (solid line).

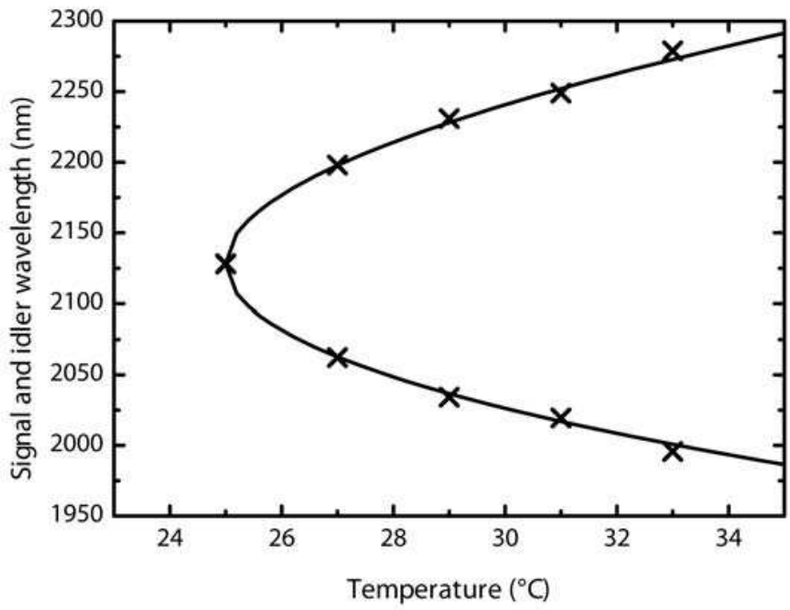

Fig. 9. Temperature tuning for λ_P = 1062 nm: experimental data (crosses) and calculated curve (solid line).

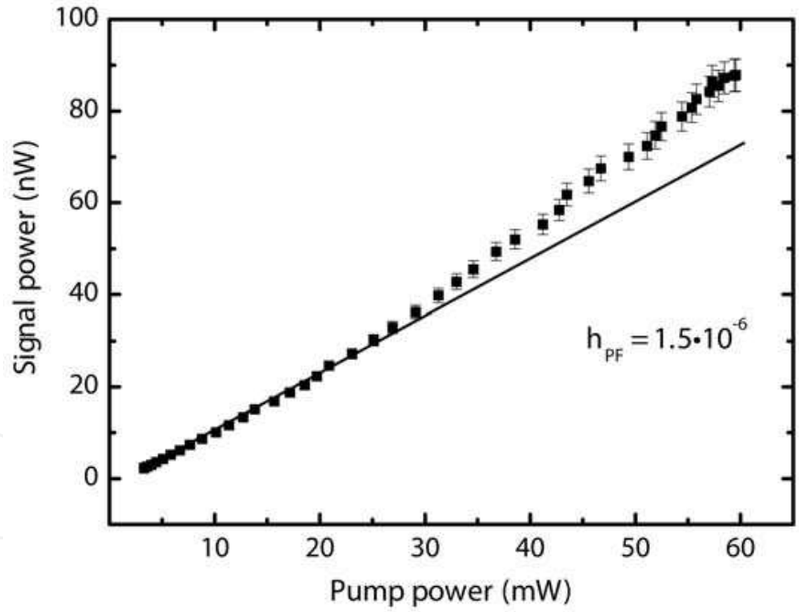

Fig. 10. Generated signal versus pump power: the nonlinear trend of experimental data (squares) is pointed out by the linear fit of the low power points (solid line).

Figure 10 shows the generated signal as a function of the TM coupled pump power P_p at degeneracy, where both vacuum fluctuations effective input and parametric gain coefficient are maximum. The latter can be written as

$$g = \sqrt{8\pi^2 |\Gamma|^2 P_p / \left(n_p n_i n_s \lambda_i \lambda_s \varepsilon_0 c\right)} \tag{12}$$

with

$$\Gamma = \int d_{14}(\rho)\Phi_p(\rho)\Phi_s(\rho)\Phi_i(\rho)d\rho \quad (13)$$

the nonlinear overlap integral of the interacting mode profiles $\Phi_{p,s,i}$, ρ a vector in the transverse plane, ε_0 the vacuum permittivity, c the velocity of light, $n_{p,s,i}$ the effective indices, $\lambda_{p,s}$ the wavelengths, and subscripts p, s, i indicating pump, signal and idler, respectively.
Generated signal is expected to grow as the parametric gain at phase-matching $G = \sinh^2(gL)$, thus staying approximately linear in the low gain regime ($gL<1$), when $G \approx (gL)^2$ (Boyd, 2008). Thanks to the high quality of the sample, maximum coupled pump, which is limited by input facet optical damage, reached in this case 60 mW. Accordingly, signal power went beyond such low-gain regime, showing the onset of a nonlinear dependence on P_p and reaching a maximum of 100 nW, with an internal conversion efficiency $P_s/P_p = (1.5\pm0.2)10^{-6}$.

5.2 Parametric amplification

Parametric amplification was demonstrated on a similar sample, with phase-matching at degeneracy shifted at 1030 nm by using slightly thinner GaAs layers in the core (255 nm). As for parametric fluorescence, experiments were performed at degeneracy, where parametric gain and phase-matching bandwidth are maximum. The pump beam was provided by an Yb:YAG mono-mode CW laser slightly tunable around 1.03 μm. The signal was obtained by mixing in a PPLN crystal a part of the same Yb:YAG beam with a narrow-line (1.5 GHz), CW Ti:Sapphire laser around 0.7 μm. At the PPLN output, the so obtained beam at the difference frequency, i.e. at $\lambda_s \approx 2$ μm, is singled-out by means of a Ge filter.

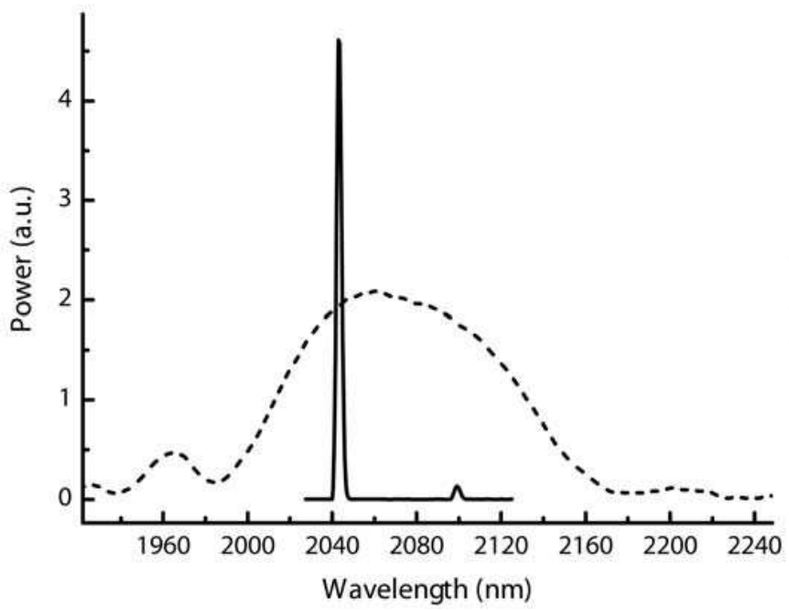

Fig. 11. Waveguide output spectra: amplified signal and idler (solid line) resulting from pump and signal simultaneous coupling, and parametric fluorescence obtained with the only input pump (dashed line).

At first, only the 100 mW (external power) TM polarized pump beam at λ_p = 1036 nm was injected in the waveguide. The resulting parametric fluorescence spectrum was acquired while the sample temperature was finely tuned to exactly set parametric gain at degeneracy, as shown in Figure 11 (dotted line). Then, the Ti:Sapphire wavelength and the PPLN temperature were set in order to produce a signal beam at λ_s = 2046 nm, i.e. well inside the gain band and slightly off its center, so as to spectrally resolve signal and idler outputs. The 500 μW TE signal beam was coupled into the waveguide along with the pump, obtaining the output spectrum reported in the same figure at a different scale (solid line). This shows the amplified signal and a clear idler peak at difference frequency λ_i = 2099 nm. The linewidth of the two peaks is determined by the finite resolution of the spectrometer.

Near degeneracy, where $\lambda_s \approx \lambda_i$ and $G \approx P_i(L)/P_s(L)$ in the low-gain regime, g and G can be directly evaluated by measuring the idler to signal output ratio. In this case, in addition, $P_i(L)$ and $P_s(L)$ can be measured with the same detector, so that their ratio is not affected by calibration uncertainties.

Figure 12 shows the idler-to-signal ratio vs. TM coupled pump power P_p, which is well fitted by a straight line as expected for low-gain. The maximum parametric amplification, obtained for $P_p \approx 30$ mW, is G = 4.5 %. The slope scaled to the waveguide length L gives the normalized parametric gain coefficient $g/P^{1/2} = 4.1 \pm 0.1$ cm^{-1}W$^{-1/2}$.

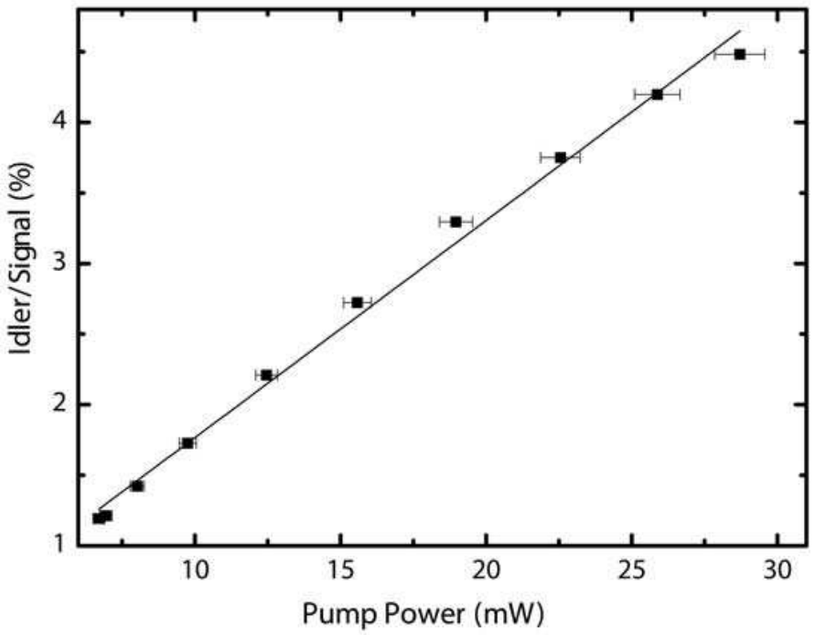

Fig. 12 Output idler-to-signal percentage, i.e. parametric amplification, vs. coupled pump power.

6. Toward an integrated optical parametric oscillator

6.1 Cavity configuration and oscillation threshold

The realization of the first GaAs-based waveguided OPO now faces the difficulties of fabricating a sufficiently resonant cavity. The first choice to deal with is the design of the

OPO cavity. Two common schemes are the singly-resonant OPO (SROPO) and the doubly-resonant OPO (DROPO). In the SROPO the cavity is resonant only at signal (idler) wavelength, i.e. $R_p \approx 0$, $R_s \approx 1$, $R_i \approx 0$ ($R_p \approx 0$, $R_s \approx 0$, $R_i \approx 1$), while in the DROPO both the generated wavelengths are resonating, i.e. $R_p \approx 0$, $R_s \approx 1$, $R_i \approx 1$. As the gain in the active medium is unidirectional, the PM condition is fulfilled only when the three waves are copropagating, signal and idler are amplified in the nonlinear crystal only in one propagation direction.
By equating cavity losses in a round trip and single-pass parametric amplification, the gain threshold for a SROPO results (Sutherland, 1996)

$$(g_{th} L)^2 \approx 2\left[1 - R_s \exp(-\alpha_s L)\right] \tag{14}$$

In a DROPO, the threshold is significantly lower:

$$(g_{th} L)^2 \approx \left[1 - R_s \exp(-\alpha_s L)\right] \left[1 - R_i \exp(-\alpha_i L)\right] \tag{15}$$

Since OPOs do not depend on a resonance of the active medium but only on frequency conservation and on the PM condition along the cavity axis, a wide spectral range is attainable, typically limited by the high-reflectivity band of the cavity mirrors.
According to the previous equations, and the typical parametric gain coefficient and propagation losses of our waveguides, the steady-state pump threshold of a SROPO is $P_p^{(th)}$=250 mW, for a waveguide length L=3 mm and a facet reflectivity R = 95%. For a DROPO in the same conditions, the pump threshold is one order of magnitude lower: $P_p^{(th)}$=23 mW. The maximum power we can couple in our waveguide, at present limited to about 70 mW, prevents the adoption of the former configuration. However, as we already mentioned, the standard loss coefficient of our nonlinear waveguides is 0.4-0.7 cm^{-1} which causes the minimum facet reflectivity required to vary. For a symmetric integrated resonator, with equal signal and idler losses, the pump power threshold in a DROPO is:

$$P_p^{(th)} = \frac{1}{\eta_{norm}} \left[\frac{\alpha_p / 2}{1 - \exp(-\alpha_p L / 2)} \ln\left(Q + \sqrt{Q^2 - 1} \right) \right]^2 \tag{16}$$

where η_{norm} is the waveguide normalized conversion efficiency and

$$Q = \frac{1 + R_s R_i \exp(-2\alpha L)}{(R_s + R_i)\exp(-\alpha L)} \tag{17}$$

with $R_{s,i}$ the facet reflectivity at the signal and idler wavelength, and α the signal and idler losses. Figure 13 shows the variation of $P_p^{(th)}$ with the facet reflectivity for a typical 3 mm-long waveguide. For the typical values of the propagation losses, the minimum reflectivity required ranges between 84 and 95%.

6.2 Design and fabrication of the integrated mirrors

The solution we have adopted to place our nonlinear waveguide in a DROPO resonator is the deposit of multilayer dielectric mirrors on the facets. However, such deposit on GaAs/AlOx waveguides is made difficult by a 12% contraction of AlAs layers during oxidation. This contraction causes an irregular surface of the waveguide facets (Durand et

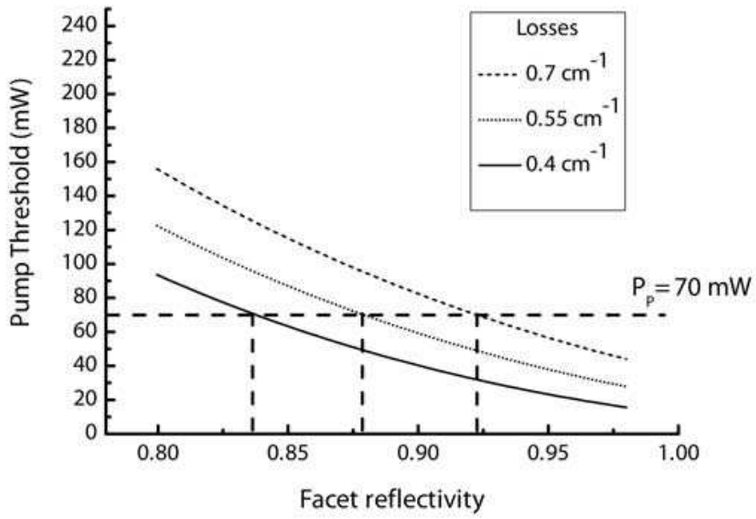

Fig. 13. Calculated pump threshold vs. facet reflectivity, where P_p=70mW corresponds to the waveguides damage threshold.

al., 2003). Moreover, such shrinkage results in a mechanical stress for the whole waveguide structure, making the adhesion of coating more critical.

Accordingly, the choice of the materials to deposit has mainly been dictated by the reduction of the total coating thickness. We have tested two material combinations: Si and low-index Al_2O_3 on the one side and YF_3 and ZnS on the other side.

Three criteria were taken into account for the design of the mirrors. First, we set the signal and idler reflectivity as high as possible. Second, we set the pump reflectivity as low as possible in order to be able to increase the coupled pump power and to prevent a resonant behaviour at λ_p which could affect the OPO stability. Finally the total thickness of the coating must be kept below 3 μm.

The mirrors have been designed with the 1D transfer matrix method (Yeh, 1988). We have optimized the thickness of individual layers with an algorithm for the minimization of a merit function taking into account the three criteria listed previously.

Figure 14 shows the simulated and experimental reflectivity spectrum for both solutions. Experimental spectra, obtained for deposits on substrates, are in good agreement with the calculated ones. $R_{s,i}$ is higher than 95% all over an interval of at least 400 nm around λ=2.0μm and R_p is lower than 15%.

The same types of multilayers have been deposited on the facets of waveguides. For each deposit we noted technologic issues. The Si/Al_2O_3 coating was detached, supposedly because of elements specific to our waveguides and experimental conditions, namely absorption in Si layers or poor adhesion of the coating to the facet. In the case of YF_3/ZnS, the adhesion on the waveguides facets was correct but we noticed the deposition of ZnS all over the samples, tending to form small clusters on the waveguides. Those clusters were responsible of additional Rayleigh scattering from the sides of the waveguides. This problem is mainly due to the evaporation of ZnS that tends to diffuse easily everywhere.

Current research is done on the deposition of other couples of materials. We also investigate the protection of the waveguides during the mirrors deposition and an effort is made on the design of a waveguide with a different geometry to isolate the propagating modes from additional scattering from edges.

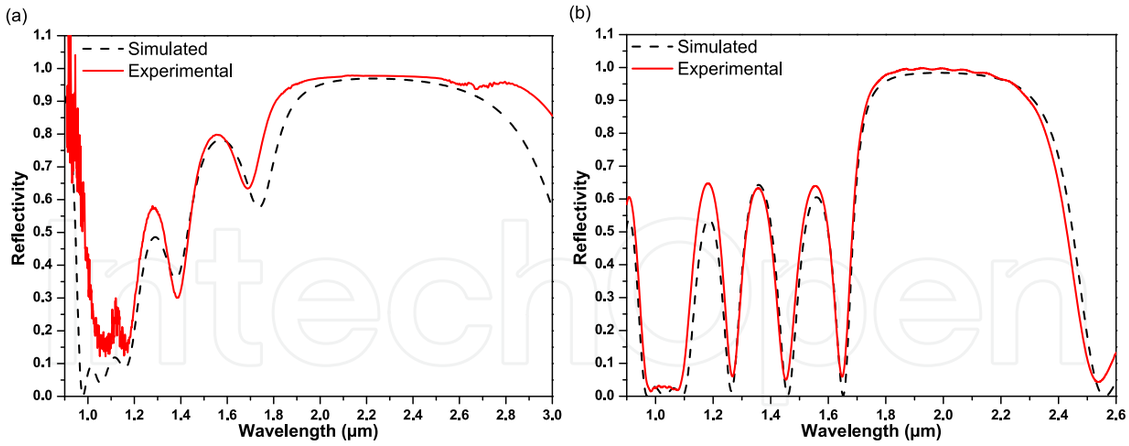

Fig. 14. Calculated and experimental reflectivity spectra for Si/Al_2O_3 (a) and YF_3/ZnS (b) coatings.

7. References

Arie, A.; Fradkin-Kashi, K. & Shreberk, Y. (2002). Frequency conversion in novel materials and its application to high resolution gas sensing. *Optics and Lasers in Engineering*, 37, 2, (February 2002) 159-170, ISSN: 0143-8166

Born, M. & Wolf, E. (1980). *Principles of optics*, Pergamon Press, ISBN: 978-0080264813, Oxford

Bortz, M. L.; Arbore, M. A. & Fejer, M. M. (1995). Quasi-phase-matched optical parametric amplification and oscillation in periodically poled $LiNbO_3$ waveguides. *Optics Letters*, 20, 1, (January 1995) 49-51, ISSN: 0146-9592

Boyd, R. W. (2008). *Nonlinear Optics*, Academic Press, ISBN: 978-0123694706, Boston

Bravetti, P.; Fiore, A.; Berger, V.; Rosencher, E.; Nagle, J. & Gauthier-Lafaye, O. (1998). 5.2–5.6 μm source tunable by frequency conversion in a GaAs-based waveguide, *Optics Letters*, 23, 5, (March 1998) 331-333, ISSN: 0146-9592

Chen, W. D.; Burie, J. & Boucher, D. (1999). Mid-infrared generation by optical frequency conversion and applications to spectroscopy and air monitoring. *Spectrochimica Acta A*, 55, 10, (September 1999) 2057-2075, ISSN: 1386-1425

Dallesasse, J. M.; Holonyak, N.; Sugg, A. R.; Richard, T. A. & El-Zein, N. (1990a). Hydrolyzation oxidation of $Al_xGa_{1-x}As$-AlAs-GaAs quantum-well heterostructures and superlattices. *Applied Physics Letters*, 57, 26, (December 1990) 2844-2446, ISSN: 0003-6951

Dallesasse, J. M.; Gavrilovic, P.; Holoniak Jr., N.; Kaliski, R. W.; Nam, D. W.; Vesely, E. J. & Burnham, R. D. (1990b). Stability of AlAs in $Al_xGa_{1-x}As$-AlAs-GaAs quantum-well heterostructures. *Applied Physics Letters*, 56, 24, (June 1990) 2436-2438, ISSN: 0003-6951

De Rossi, A.; Berger, V.; Calligaro, M.; Leo, G.; Ortiz, V. & Marcadet, X. (2001). Parametric fluorescence in oxidized aluminium gallium arsenide waveguides. *Applied Physics Letters*, 79, 23, (December 2001) 3758-3760, ISSN: 0003-6951

De Rossi, A.; Berger, V.; Leo, G. & Assanto, G. (2005a). Form birefringence phase matching in multilayer semiconductor waveguides: tuning and tolerances. *IEEE Journal of Quantum Electronics*, 41, 10, (October 2005) 1293-1302, ISSN: 0018-9197

De Rossi, A.; Ortiz, V.; Calligaro, M.; Lanco, L.; Ducci, S.; Berger, V. & Sagnes, I. (2005b). Measuring propagation loss in a multimode semiconductor waveguide. Journal of Applied Physics, 97, 7, (March 2005) 073105-1-073105-7, ISSN: 0021-8979

Durand, O.; Wyckzisk, F.; Olivier, J.; Magis, M.; Galtier, P.; De Rossi, A.; Calligaro, M.; Ortiz, V.; Leo, G. & Assanto, G. (2003). Contraction of aluminum oxide thin layers in optical heterostructures. *Applied Physics Letters*, 83, 13, (September 2003) 2554-2556, ISSN: 0003-6951

Eyres, L. A.; Tourreau, P. J. ; Pinguet, T. J.; Ebert, C. B.; Harris, J. S.; Fejer, M. M. ; Becouarn, L.; Gerard, B. & Lallier, E. (2001). All-epitaxial fabrication of thick, orientation patterned GaAs films for nonlinear optical frequency conversion. *Applied Physics Letters*, 79, 7, (August 2001) 904-906, ISSN: 0003-6951

Fiore, A.; Berger, V.; Rosencher, E.; Bravetti, P.; Laurent, N. & Nagle, J. (1997). Phasematched mid-infrared difference frequency generation in GaAs-based waveguides. *Applied Physics Letters*, 71, 25, (December 1997) 3622-3624, ISSN: 0003-6951

Fiore, A.; Berger, V.; Rosencher, E.; Bravetti, P. & Nagle, J. (1998a). Phase-matching using an isotropic nonlinear material. *Nature* 391, 6691, (January 1998) 463-466, ISSN: 0028-0836

Fiore, A.; Sanz, J.; Delobel, L.; van der Meer, P.; Bravetti, P.; Berger, V.; Rosencher, E. & Nagle, J. (1998b). Second-harmonic generation at λ= 1.6 μm in AlGaAs/Al_2O_3 waveguides using birefringence phase matching. *Applied Physics Letters*, 72, 23, (June 1998) 2942-2944, ISSN: 0003-6951

Gehrsitz, S.; Reinhart, F. K.; Gourgon, C.; Herres, N.; Vonlanthen, A. & Sigg, H. (2000). The refractive index of $Al_xGa_{1-x}As$ below the band gap: Accurate determination and empirical modelling. *Journal of Applied Physics*, 87, 11, (June 2000) 7825-7837, ISSN: 0021-8979

Gisin, N.; Ribordy, G.; Tittel, T. & Zbinden, H. (2002). Quantum Criptography. *Review of Modern Physics*, 74, 1, (January 2002) 145-195, ISSN: 0034-6861

Goodnick, S. M.; Ferry, D. K.; Wilmsen, C. W.; Liliental, Z.; Fathy, D. & Krivanek, O. L. (1985). Surface roughness at the Si(100)-SiO_2 interface, *Physical Review B*, 32, 12, (December 1985) 8171-8186, ISSN: 1098-0121

Hall, D. C.; Wu, H.; Kou, L.; Luo, Y.; Epstein, R. J.; Blum, O. & Hou, H. (1999). Refractive index and hygroscopic stability of $Al_xGa_{1-x}As$ native oxides. *Applied Physics Letters*, 75, 8, (August 1999) 1110-1112, ISSN: 0003-6951

Hofer, F.; Warbichler, P. & Grogger, W. (1995). Imaging of nanometer-sized precipitates in solids by electron spectroscopic imaging. *Ultramicroscopy*, 59, 1-4, (July 1995) 15-31, ISSN: 0304-3991

Hofmann, D.; Schreiber, G.; Grundkötter, W.; Ricken, R. & Sohler, W. (2000) Mid-infrared continuous-wave singly resonant optical parametric oscillator with periodically poled Ti:$LiNbO_3$ waveguide, *Conference on Lasers and Electro-Optics Europe*, paper CDM4, ISBN: 0-7803-6319-1, Nice, September 2000, IEEE

Kintaka, K.; Fujimura, M.; Suhara, T. & Nishihara, H. (1996). High-efficiency $LiNbO_3$ waveguide second-harmonic generation devices with ferroelectric-domain-inverted

gratings fabricated by applying voltage. *Journal of Ligthwave Technology*, 14, 3 (March 1996), 462-469, ISSN: 0733-8724

Knopp, K. J.; Mirin, R. P.; Christensen, D. H.; Bertness, K. A.; Roshko, A. & Synowicki, R. A. (1998). Optical constants of $(Al_{0.98}Ga_{0.02})_xO_y$ native oxides. *Applied Physics Letters*, 73, 24 (December 1998) 3512-3514, ISSN: 0003-6951

Lancaster, D. G.; Richter, D. & Tittel, F. K. (1999). Portable fiber-coupled diode-laser-based sensor for multiple trace gas detection. *Applied Physics B*, 69, 5-6, (December 1999) 459-465, ISSN: 1432-0649

Lacey, J. P. R. & Payne, F. P. (1990). Radiation loss from planar waveguides with random wall imperfections. *IEE Proceedings*, 137, 4, (August 1990) 282-288, ISSN: 1350-2433

Moutzouris, K.; Rao, S. V.; Ebrahimzadeh, M.; De Rossi, A.; Berger, V.; Calligaro, M. & Ortiz, V. (2001). Efficient second-harmonic generation in birefringently phase-matched GaAs/Al_2O_3 waveguides. *Optics Letters*, 26, 22, (November 2001) 1785-1787, ISSN: 0146-9592

Ravaro, M.; Le Dû, M.; Likforman, J.-P.; Ducci, S.; Berger, V. & Leo, G. (2007). Estimation of parametric gain in GaAs/AlOx waveguides by fluorescence and second harmonic generation measurements, *Applied Physics Letters*, 91, 19, (November 2007) 191110-1-191110-3, ISSN: 0003-6951

Ravaro, M.; Guillotel, E.; Le Dû, M.; Manquest, C.; Marcadet, X.; Ducci, S.; Berger, V. & Leo, G. (2008). Nonlinear measurement of mid-IR absorption in AlOx waveguides. *Applied Physics Letters*, 92, 15,(April 2008) 151111-1-151111-3, ISSN: 0003-6951

Scaccabarozzi, L.; Fejer, M. M.; Huo, Y.; Fan, S.; Yu, X. & Harris, J. S. (2006). Enhanced second-harmonic generation in AlGaAs/Al_xO_y tightly confining waveguides and resonant cavities. *Optics Letters*, 31, 24, (December 2006) 3626-3628, ISSN: 0146-9592

Sergienko, A. & Jaeger, G. S. (2003). Quantum information processing and precise optical measurement with entangled-photon pairs, *Contemponary Physics*, 44, 4, (July 2003) 341-356, ISSN: 1366-5812

Sorokina, I. T. & Vodopyanov, K. L. (2003). *Solid-State Mid-Infrared Laser Sources*, Springer, ISBN: 978-3540006213, New-York

Sutherland, R. L. (2003). *Handbook of Nonlinear Optics*, Marcel Dekker, ISBN: 978-0824742435, New York

Venugopal Rao, S.; Moutzouris, K.; Ebrahimzadeh, M.; De Rossi, A. ; Gintz, G.; Calligaro, M.; Ortiz, V. & Berger, V. (2003). Influence of scattering and two-photon absorption on the optical loss in GaAs/Al_2O_3 nonlinear waveguides measured using femtosecond pulses. *IEEE Journal of Quantum Electronics*, 39, 3, (March 2003) 478-486, ISSN: 0018-9197

Vodopyanov, K. L.; Levi, O.; Kuo, P. S.; Pinguet, T. J.; Harris, J. S.; Fejer, M. M.; Gerard, B.; Becouarn, L. & Lallier, E. (2004). Optical parametric oscillation in quasi-phase-matched GaAs, *Optics Letters*, 29, 16, (August 2004) 1912-1914, ISSN: 0146-9592

Yeh, P. (1988). *Optical waves in layered media*. Wiley, ISBN: 978-0471828662, New York

Yoo, S. J. B. (1996). Wavelength conversion technologies for WDM network applications. *Journal of Ligthwave and Technology*, 14, 6, (June 1996) 955-966, ISSN: 0733-8724

Yu, X.; Scaccabarozzi, L.; Harris Jr., J. S.; Kuo, P. S. & Fejer, M. M. (2005) Efficient continuous wave second harmonic generation pumped at 1.55 μm in quasi-phase-matched AlGaAs waveguides, *Opt. Express* 13, 26, (December 2005) 10742-10748, ISSN: 1094-4087

van der Ziel, J. P. (1975). Phase-matched Harmonic Generation in a Laminar Structure with Wave Propagation in the plane of the Layers, *Applied Physics Letters*, 26, 2, (January 1975) 60-61, ISSN: 0003-6951

van der Ziel, J. P. & Gossard, A. C. (1978). Optical birefringence of ultrathin AlGaAs-GaAs Multilayer Heterostructures. *Journal of Applied Physics*, 49, 5, (May 1978) 2919-2921, ISSN: 0021-8979

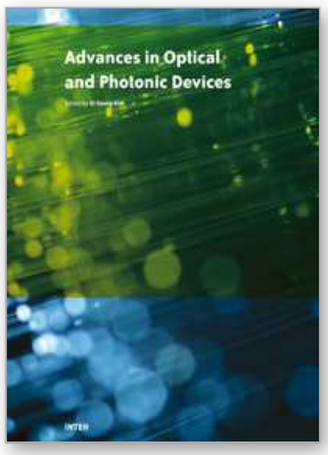

Advances in Optical and Photonic Devices

Edited by Ki Young Kim

ISBN 978-953-7619-76-3
Hard cover, 352 pages
Publisher InTech
Published online 01, January, 2010
Published in print edition January, 2010

The title of this book, Advances in Optical and Photonic Devices, encompasses a broad range of theory and applications which are of interest for diverse classes of optical and photonic devices. Unquestionably, recent successful achievements in modern optical communications and multifunctional systems have been accomplished based on composing “building blocks” of a variety of optical and photonic devices. Thus, the grasp of current trends and needs in device technology would be useful for further development of such a range of relative applications. The book is going to be a collection of contemporary researches and developments of various devices and structures in the area of optics and photonics. It is composed of 17 excellent chapters covering fundamental theory, physical operation mechanisms, fabrication and measurement techniques, and application examples. Besides, it contains comprehensive reviews of recent trends and advancements in the field. First six chapters are especially focused on diverse aspects of recent developments of lasers and related technologies, while the later chapters deal with various optical and photonic devices including waveguides, filters, oscillators, isolators, photodiodes, photomultipliers, microcavities, and so on. Although the book is a collected edition of specific technological issues, I strongly believe that the readers can obtain generous and overall ideas and knowledge of the state-of-the-art technologies in optical and photonic devices. Lastly, special words of thanks should go to all the scientists and engineers who have devoted a great deal of time to writing excellent chapters in this book.

InTech Europe
University Campus STeP Ri
Slavka Krautzeka 83/A
51000 Rijeka, Croatia
Phone: +385 (51) 770 447

InTech China
Unit 405, Office Block, Hotel Equatorial Shanghai
No.65, Yan An Road (West), Shanghai, 200040, China
中国上海市延安西路65号上海国际贵都大饭店办公楼405单元
Phone: +86-21-62489820

Fax: +385 (51) 686 166
www.intechopen.com

Fax: +86-21-62489821

IntechOpen